Biophysical Journal
Article

Biophysical Society

Measuring Mobility in Chromatin by Intensity-Sorted FCS

Melody Di Bona,[1,2] Michael A. Mancini,[3] Davide Mazza,[4,5] Giuseppe Vicidomini,[6] Alberto Diaspro,[1,2,*] and Luca Lanzanò[1,*]

[1]Nanoscopy and Nikon Imaging Center, Istituto Italiano di Tecnologia, Genoa, Italy; [2]Department of Physics, University of Genoa, Genoa, Italy; [3]Department of Molecular and Cellular Biology, Baylor College of Medicine, Houston, Texas; [4]Experimental Imaging Center Ospedale San Raffaele, Milano, Italy; [5]The European Center for Nanomedicine, Milano, Italy; and [6]Molecular Microscopy and Spectroscopy, Istituto Italiano di Tecnologia, Genoa, Italy

ABSTRACT The architectural organization of chromatin can play an important role in genome regulation by affecting the mobility of molecules within its surroundings via binding interactions and molecular crowding. The diffusion of molecules at specific locations in the nucleus can be studied by fluorescence correlation spectroscopy (FCS), a well-established technique based on the analysis of fluorescence intensity fluctuations detected in a confocal observation volume. However, detecting subtle variations of mobility between different chromatin regions remains challenging with currently available FCS methods. Here, we introduce a method that samples multiple positions by slowly scanning the FCS observation volume across the nucleus. Analyzing the data in short time segments, we preserve the high temporal resolution of single-point FCS while probing different nuclear regions in the same cell. Using the intensity level of the probe (or a DNA marker) as a reference, we efficiently sort the FCS segments into different populations and obtain average correlation functions that are associated to different chromatin regions. This sorting and averaging strategy renders the method statistically robust while preserving the observation of intranuclear variations of mobility. Using this approach, we quantified diffusion of monomeric GFP in high versus low chromatin density regions. We found that GFP mobility was reduced in heterochromatin, especially within perinucleolar heterochromatin. Moreover, we found that modulation of chromatin compaction by ATP depletion, or treatment with solutions of different osmolarity, differentially affected the ratio of diffusion in both regions. Then, we used the approach to probe the mobility of estrogen receptor-α in the vicinity of an integrated multicopy prolactin gene array. Finally, we discussed the coupling of this method with stimulated emission depletion FCS for performing FCS at subdiffraction spatial scales.

INTRODUCTION

Chromatin is a macromolecular complex mainly composed by DNA and histones. Chromatin not only has the function of compacting the DNA to make it fit into the nucleus but also plays an active role in the regulation of all biological processes using DNA as a template in eukaryotes, such as transcription, DNA replication, and DNA repair. The spatial and temporal organization of chromatin is often deeply perturbed in diseases such as cancer, leading to misregulation of these processes and, for example, to aberrant gene expression profiles. From a microscopic point of view, transcription requires the coordination in time and space of multiple macromolecular complexes so that they can quickly assemble over an accessible DNA responsive element. Moreover, early experiments clearly established that transcription factors and other nuclear protein interactions were more dynamic than expected (1,2). Thus, it remains fundamentally important to determine how proteins move within different regions of the nucleus that are comprised of markedly heterogeneous chromatin density and maintain their ability to reach and bind to their target sequences (3).

In this field, a critical role has been played by fluorescence microscopy methods developed to study molecular mobility, including fluorescence recovery after photobleaching (4), fluorescence correlation spectroscopy (FCS) (5), and single-molecule tracking (6). These techniques have made it possible to investigate dynamic processes within the nuclei of living cells, retrieving information about chromatin dynamics, structure, and interactions (7–11). In particular, FCS is based on the analysis of fluorescence intensity fluctuations arising from the passage of fluorescent molecules through a small observation volume (~1 fL). The average amplitude and duration of the fluctuations,

Submitted October 24, 2018, and accepted for publication February 8, 2019.

*Correspondence: alberto.diaspro@iit.it or luca.lanzano@iit.it

Editor: Jochen Mueller.

https://doi.org/10.1016/j.bpj.2019.02.003

extracted from the autocorrelation function (ACF) of the intensity signal, provide information on the concentration and the mobility of the fluorescent particles. FCS is typically implemented in confocal microscopes and possesses a high temporal resolution and the sensitivity of a single-molecule method, although without the constraint of having only a few molecules labeled in the field of view; moreover, it induces less photodamage to the cells than perturbation methods (12,13). For these reasons, FCS has been widely used for measurements in the nucleus and has been shown to be useful for retrieving information on the nuclear environment in an indirect way (i.e., using an inert probe), for studying the motion of molecules interacting with chromatin, and for measuring the mobility of chromatin itself (8,14–20). In this approach, both the structural and dynamic aspects of the nucleus biology can be investigated, providing a more integrated view of nuclear structure and function.

It is important to determine whether variations in the architectural organization of chromatin have a significant impact on the diffusion of surrounding molecules. To answer this question and to characterize protein mobility in different chromatin regions, several strategies have been proposed that add spatial information to the single-point FCS measurement. Maps of diffusion coefficients have been obtained, for instance, by sequential acquisition of single-point FCS measurements (21,22), by light-sheet illumination (23,24), or by parallel acquisition of FCS data at multiple observation volumes (25,26). Another method that has been used to measure fluctuations at and between different points in the nucleus is scanning FCS, which is easily implemented on confocal laser scanning microscopes but whose temporal resolution is typically limited by scanning to the millisecond range (27,28). Finally, diffusion maps have been recently obtained from the analysis of raster image correlation spectroscopy data (29). However, these methods will only provide an accurate description of the mobility properties in different nuclear regions if they are immobile during FCS data acquisition.

A significant advantage can be gained if the different chromatin regions are identified with the help of a reference marker (30). For instance, the intensity of a fluorescent protein can be used to identify specific subnuclear regions or, simply, the intensity of a DNA marker (e.g., Hoechst) can be used to identify regions of different chromatin density (31). In this case, the reference intensity can be used as a bona fide marker to assign, during data analysis, each single-point FCS measurement to a specific chromatin region. In this respect, the acquisition of a brief FCS measurement is fundamental to ensure that the probed region does not move significantly during each measurement. On the other hand, the poor statistics resulting from a short FCS acquisition must be compensated by averaging over many FCS measurements assigned to the same chromatin region.

Here, we implemented this idea by performing a slow circular scanning of the excitation beams across the nucleus. The fluctuation analysis is performed by dividing the whole acquisition into a large number of short temporal segments and considering each segment like an independent FCS measurement, tagged with an intensity value of the reference marker. The ACFs calculated from these short segments are first sorted into two or more populations, corresponding to specific chromatin regions, and then averaged. As a result, this intensity-sorted FCS approach yields, for each measurement, an ACF associated to each chromatin region. In addition, because each measurement is acquired from a single cell, it is possible to measure the dynamic properties of different compartments cell by cell, thus avoiding the intracellular mobility differences being distorted because of the intercellular variability.

We validated the technique by measuring differences in the diffusion coefficient of the green fluorescent protein (GFP) in the nucleolus and in the nucleoplasm of live HeLa cells using, as a reference, the relative intensity variation of GFP in the two compartments. Then, we applied the technique to detect differences of GFP diffusion between regions of hetero- and euchromatin, using Hoechst staining of DNA as the reference. We found that the mobility of GFP is reduced in the heterochromatin regions, especially in the perinucleolar heterochromatin. This is, to the best of our knowledge, the first time that such a reduction in mobility is observed for a small, inert probe like the monomeric GFP. The ratio between the diffusion coefficient in hetero- versus euchromatin was monitored upon treatments affecting chromatin compaction. We found that compaction because of ATP depletion or hyperosmolar treatment affected this ratio in different ways. In addition, we measured the mobility of the estrogen receptor-α (ER) on or away from an engineered transcription locus. Finally, we showed that the approach can be combined with stimulated emission depletion (STED)-FCS to obtain subdiffraction spot-variation FCS data in specific nuclear regions.

MATERIALS AND METHODS

Implementation of intensity-sorted FCS

The schematic implementation of the method is depicted in Fig. 1, *a–c*. The excitation volume of a confocal microscope is slowly scanned across the specimen (Fig. 1 *a*) while the fluorescence intensity from one or more spectral channels is continuously recorded at a high temporal resolution (Fig. 1 *b*). The scan can have any pattern as long as the scanning speed is low. In particular, here, we use a circular scanning path (Fig. 1 *a*), similar to what is done in orbital scanning (32,33) but at a much lower scanning frequency. The whole intensity trace I recorded in one channel is divided into short temporal sequences, or segments, of duration T_{seg}, and from each segment a short-sequence (ss) ACF is calculated (Fig. 1 *b*). Then the ssACFs are sorted based on the value of intensity I_s associated to each segment (Fig. 1 *c*). The intensity I_s used for sorting the ACFs can be the intensity recorded in the same or in another channel. For instance, if the orbit is scanned across two distinct regions (Fig. 1 *a*), detectable by

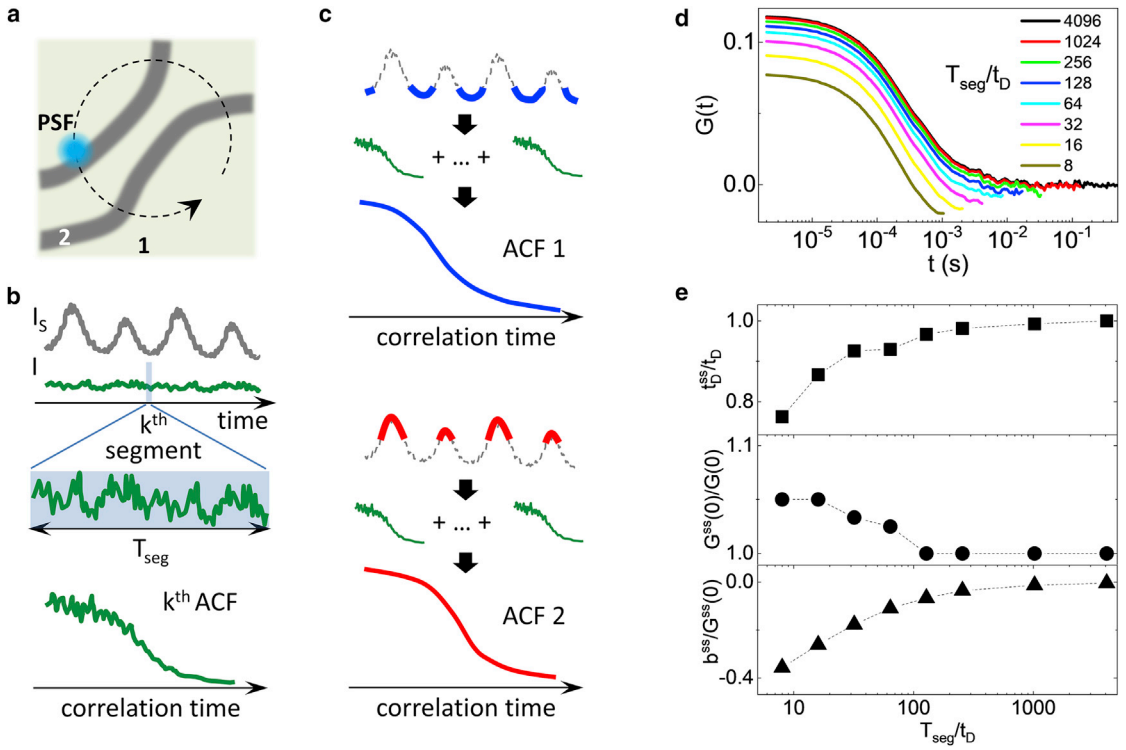

FIGURE 1 (*a–c*) Schematic implementation of the method. A confocal spot (PSF) is slowly scanned in a circular path across the specimen (*a*), and the fluorescence from one or more channels is continuously recorded (*b*). The whole measurement is divided into short segments of duration T_{seg}, and for each segment, the corresponding ACF is calculated (*b*). The ACFs are then sorted into two or more populations, based upon the value of the reference intensity I_s, and for each population, the average ACF is calculated (*c*). (*d*) Short-sequence (ss) ACFs are calculated from simulated data for different values of T_{seg}/t_D. (*e*) Deviation of the fitting parameters (Eq. 1) of the ssACF for different values of T_{seg}/t_D is shown. To see this figure in color, go online.

a difference in the intensity I_s (Fig. 1 *b*), one can obtain an ACF associated to each region by averaging only the ssACFs corresponding to segments whose intensity is below or above a given threshold, respectively (Fig. 1 *c*).

The duration T_{seg} of the segments must be short enough to resolve intensity variations in the sorting intensity channel I_s but long enough to properly sample fluorescence intensity fluctuations and prevent deformation of the ACFs. To estimate a reasonable lower limit for T_{seg}, we simulated molecules undergoing Brownian motion with diffusion coefficient D through a Gaussian observation volume of lateral waist w and axial waist $w_z >> w$. We divided the resulting intensity trace in segments of duration T_{seg}, and then the ssACF was calculated and averaged over all segments. The extent of the deformation of the ACF depends on the ratio between T_{seg} and the characteristic time of the fluctuations, $t_D = w^2/4D$ (Fig. 1 *d*). The deformations of the undersampled ACF were quantified by fitting each ACF to the following function:

$$G^{ss}(t) = G^{ss}(0)\left(1+\frac{t}{t_D^{ss}}\right)^{-1} + b^{ss}. \quad (1)$$

The fitting parameters of the undersampled ACF were then compared with those of the ACF calculated with an infinite sampling time. The ACF calculated with an infinite sampling time was fitted to the following function:

$$G(t) = G(0)\left(1+\frac{t}{t_D}\right)^{-1} + b, \quad (2)$$

where b is set to 0. For shorter values of T_{seg}, the ACF are characterized by shorter values of t_D^s, negative values of b^s, and slightly larger values of the amplitude $G^s(0)$. We can consider $T_{seg} \sim 10^2 t_D$ as a lower limit for the duration of the ss. In fact, for $T_{seg} > 10^2 t_D$, the more meaningful parameters t_D and G(0) deviate by less than 5%, in keeping with the rule of thumb that the acquisition time of FCS data has to be at least two orders of magnitude longer than the characteristic correlation time (34).

Another point to take into account is how slow we must scan to ignore the correlations due to the motion of the beam. The complete ACF function that describes a model of free diffusion in circular scanning FCS is given by (12):

$$G(t) = G(0)\left(1+\frac{t}{t_D}\right)^{-1} \exp\left(-\frac{\frac{4R^2}{w_0^2}\sin^2\left(\frac{vt}{2R}\right)}{1+\frac{t}{t_D}}\right), \quad (3)$$

where R is the radius of the orbit, and v is the scanning speed, given by $v=2\pi R/T$, where T is the period of the orbit. In our case, because we sample many segments along the orbit, $t < T_{seg} << T$, we can rewrite Eq. 3 as

$$G(t) = G(0)\left(1+\frac{t}{t_D}\right)^{-1} \exp\left(-\frac{\frac{v^2t^2}{w_0^2}}{1+\frac{t}{t_D}}\right). \quad (4)$$

We can ignore the correlations due to the motion of the scanner whenever $v^2t^2/{w_0}^2 << 1+t/t_D$, namely when $v^2 << {w_0}^2/t^2+{w_0}^2/(t_D t)$. This condition is certainly satisfied if $v << w_0/T_{seg}$ and $v^2 << {w_0}^2/(t_D T_{seg})$. Assuming $T_{seg} = 10^2 t_D$, the latter condition can also be written as $v << 0.4D/w_0$. This relation can be used to determine how slow one should scan, whatever the scan pattern. For instance, for $D \approx 20\ \mu m^2/s$ and $w_0 \approx 200$ nm, $v << 40\ \mu m/s$. For an orbit

diameter of ~3 μm, this corresponds to a scanning frequency $f << 4$ Hz. For comparison, a conventional circular scanning FCS (i.e., in which temporal correlation is performed between subsequent lines) should be run at a frequency larger than $1/t_D \approx 2$ kHz to measure diffusion in the same range.

Simulations

All the simulations were performed using SimFCS (available at http://www.lfd.uci.edu/).

Optical setup

The measurements were performed on a custom microscope, obtained from the modification of a previous setup (35). The excitation at 485 nm was provided by a pulsed laser line (LDH-D-C-485, 80 MHz; PicoQuant, Berlin, Germany), whereas the excitation at 407 nm was provided by a continuous-wave (CW) diode laser (Cube 1069413/AQ407 nm/50 mW; Coherent, Santa Clara, CA). The STED beam was generated by a CW optical pumped semiconductor laser emitting at 577 nm (Genesis CX STM-2000; Coherent). The laser power was measured at the objective back aperture.

The beams were combined and coaligned using different laser beam dichroic mirrors and then deflected by two galvanometric scanning mirrors (6215HM40B; Cambridge Technologies, Bedford, MA) and directed toward the 1.40 numerical aperture 100× objective (HCX PL APO 100/1.40/0.70 Oil; Leica Microsystems, Wetzlar, Germany) by the same set of scan and tube lenses as the ones used in a commercial scanning microscope (Leica TCS SP5; Leica Microsystems). The fluorescence light was collected by the same objective lens, descanned, passed through the laser beam dichroic mirrors, and then separated by a fluorescence beam splitter in two channels (detection bands 525/50 and 445/45 nm) before being focused (focal length 60 mm, AC254-060-AML; Thorlabs, Newton, NJ) into fiber pigtailed single-photon avalanche diodes (PDM Series; Micro Photon Devices, Bolzano, Italy). All imaging operations were automated and managed by the software ImSpector (Max Planck Innovation, München, Germany) with the exception of circular scanning, managed by the software SimFCS. For FCS measurements, photons were detected by a time-correlated single-photon counting (TCSPC) card (SPC-830; Becker & Hickl, Berlin, Germany), synchronized with the reference signal provided by the pulsed diode laser.

Cell culture

A stable HeLa cell line expressing the protein AcGFP1 was used for all the untagged-GFP experiments (36). The cells were cultured in Dulbecco's modified Eagle's medium (DMEM) supplemented by 10% fetal bovine serum, 2 mM glutamine, 100 U penicillin, and 0.1 mg/mL streptomycin (Sigma-Aldrich, St. Louis, MO).

For the ER experiments, we used a stable HeLa cell line with a 100-copy integration of the estrogen-responsive unit of the prolactin gene (Sharp et al.), which stably expresses a GFP-tagged version of ER (GFP-ERα:PRL-HeLa cell line) (37).

The GFP-ERα:PRL-HeLa cell line was grown in high-glucose DMEM without phenol red, supplemented with 5% charcoal dextran-stripped tetracycline-free fetal bovine serum, 200 μg/mL hygromycin B, and 0.8 μg/mL blasticidin S (Thermo Fisher Scientific, Waltham, MA) and 1 nM Z-4-Hydroxytamoxifen (Sigma-Aldrich).

The day before the experiment, freshly split cells were plated on eight-well chamber plates (glass bottom, thickness 170 ± 5 μm) (ibidi, Planegg, Germany) and grown overnight.

Treatments

Nuclear staining was performed incubating the cells for 15 min at 37°C with a solution of Hoechst 33342 (Thermo Fisher Scientific; stock solution 20 mM) in phosphate-buffered saline (PBS), at a final concentration of 4 μM. The cells were then washed four times with PBS 1×.

Energy depletion was obtained incubating the cells for 30 min at 37°C with DMEM supplemented with 50 mM 2-deoxyglucose (Sigma-Aldrich) and 10 mM sodium azide (Sigma-Aldrich) (38). Cells were then imaged directly in ATP depletion medium.

Treatment with solutions of different osmolarity was performed by the addition to the cell of hypo- (190 mOsm) or hyperosmolar (570 mOsm) solutions for 15 min at 37°C (39): the cells were then imaged directly in the incubation solution.

The Sheila cells were treated with 10 nM 17-β-estradiol (E2; Sigma-Aldrich) diluted in Live Cell Imaging Solution (Thermo Fisher Scientific) for 1 h to trigger the GFP-ER binding to the array and then imaged directly in the same incubation solution.

In all the other cases, measurements were performed on cells kept in Live Cell Imaging Solution.

Experiments

Cumulative results were obtained by performing from two to five independent experiments. In each experiment, we probed a number of cells varying from 5 to 30. Each measurement was performed on a different cell. All the measurements were performed by scanning a circular orbit through the cell nuclei, chosen in such a way to cross the nuclear regions of interest.

For measurements on untagged GFP, the parameters were the following: the 488 nm laser power was set to 15 μW, whereas the 405 nm laser power was set to 2.5 μW; the orbit diameter was set at 3 μm, whereas the scan period was ~16.7 s. Each measurement was recorded for 132 s.

For the ER experiments, the laser powers of the 488 and 405 nm were set at 5 and 1 μW, respectively; the orbit diameter was 1.5 μm, whereas the scan period was set to ~68 s, and each measurement lasted 264 s.

For the STED-FCS measurements, the 488 nm laser power was set to 15 μW, whereas the STED beam intensity (577 nm) was kept at 50 mW; the measurements were performed with an orbit diameter of 3 μm and a scan period of 16.7 s, whereas the whole measurement lasted 264 s.

For calibration of the effective detection volume, single-point STED-FCS was performed on a solution of purified AcGFP1 (Clontech, Mountain View, CA) in PBS as described previously (40). The measurements on solution were performed at an excitation power of 22.5 μW for a total acquisition time of 100 s.

Data analysis and fitting

Calculation of the intensity-sorted ACFs was performed in MATLAB (The MathWorks, Natick, MA). Each measurement file was first divided into segments whose duration was set based on the probe mobility; for untagged GFP, the segment duration was set to the value $T_{seg} = 131$ ms, whereas for the GFP-ER, the segment duration was set to the value $T_{seg} = 1.05$ s. For each segment, an ACF and an intensity value were calculated. The nanosecond temporal information available in the TCSPC file was used to remove the detector afterpulse in the confocal FCS data, using a custom fluorescence lifetime correlation spectroscopy routine (41). For the STED-FCS data, the nanosecond temporal information available in the TCSPC file was used to generate the multiple ACFs corresponding to subdiffraction effective volumes, as described in (40). ACFs were only calculated for the green channel because the Hoechst intensity was used only as a reference channel.

Intensity sorting was performed by averaging all the ACFs of segments whose intensity was below and/or above specific threshold values. Variations of the intensity trace due to photobleaching were removed by a nonlinear detrend before sorting.

In all the experiments with untagged GFP, the ACFs were fitted using a one-component diffusion model (Eq. 2). In the experiments with GFP-ER, the ACFs were either fitted using a two-component diffusion model

$$G(t) = G_{slow}(0)\left(1+\frac{t}{t_{D_{slow}}}\right)^{-1} + G_{fast}(0)\left(1+\frac{t}{t_{D_{fast}}}\right)^{-1} \quad (5)$$

or the diffusion and binding model (Full Model) described in (15).

For the two-component diffusion model, a global fit was performed for each experiment, keeping the two values of diffusion coefficients, D_{slow} and D_{fast}, shared between the measurements and instead letting the amplitudes vary corresponding to the fast and slow-diffusing components.

One- and two-component diffusion fits were performed in Origin. The Full Model fits were performed in MATLAB (The MathWorks).

In each independent experiment, the ratio of the diffusion coefficient in region 1 versus region 2 was estimated as the slope of a linear fit of the data through the origin. Average values of this ratio were obtained by averaging the values of slope estimated on multiple independent experiments.

Average values of diffusion coefficient were obtained by averaging values from all the measured cells across independent experiments.

RESULTS AND DISCUSSION

Measurement of the GFP diffusion in the nucleolus versus nucleoplasm

As a validation of the method, we first measured differences in the diffusion coefficient of GFP in the nucleolus and the nucleoplasm of HeLa cells. It has been previously shown that even for a small inert probe like GFP, there is a clear difference in the values of the diffusion coefficient measured in the nucleoplasm with respect to the nucleolus (26,29,42). In this case, we used the GFP intensity level as a reference marker to distinguish the two nuclear regions. In fact, the nucleolus of a cell expressing GFP appears dimmer than the nucleoplasm because of a different concentration of GFP in the two compartments (Fig. 2, *a* and *b*). The intensity trace showed easily detectable regions of low and high intensity, corresponding to the nucleolus and the nucleoplasm, respectively (Fig. 2 *c*). By specifically selecting only the short FCS segments corresponding to these low and high intensity regions (Fig. 2 *c*), we generated the sorted ACFs corresponding to the nucleolus (Fig. 2 *e*) and the nucleoplasm (Fig. 2 *f*).

By the fit of the ACF, we retrieved the average value of diffusion coefficient of GFP in the nucleolus, $D_{nl} = 8 \pm 3\ \mu m^2/s$, and in the nucleoplasm, $D_{np} = 17 \pm 5\ \mu m^2/s$ (mean ± SD of n = 73 cells from five independent experiments) (Fig. 2 *g*). These values are in keeping with the values reported in literature (26,29,42), demonstrating that our analysis method works properly. We observed a high intercellular variability in the measured absolute values of diffusion coefficient (Fig. 2, *g* and *h*). However, the ratio between the two values of diffusion coefficient in each cell is quite conserved, as shown by a D_{nl} versus D_{np} scatter plot (Fig. 2 *h*). We have evaluated this ratio by performing a linear fit of the data for each independent experiment (Fig. 2 *h*; Fig. S1). On average, we obtained $D_{nl}/D_{np} = 0.47 \pm 0.04$ (mean ± SD of five independent experiments with at least 10 different cells per experiment).

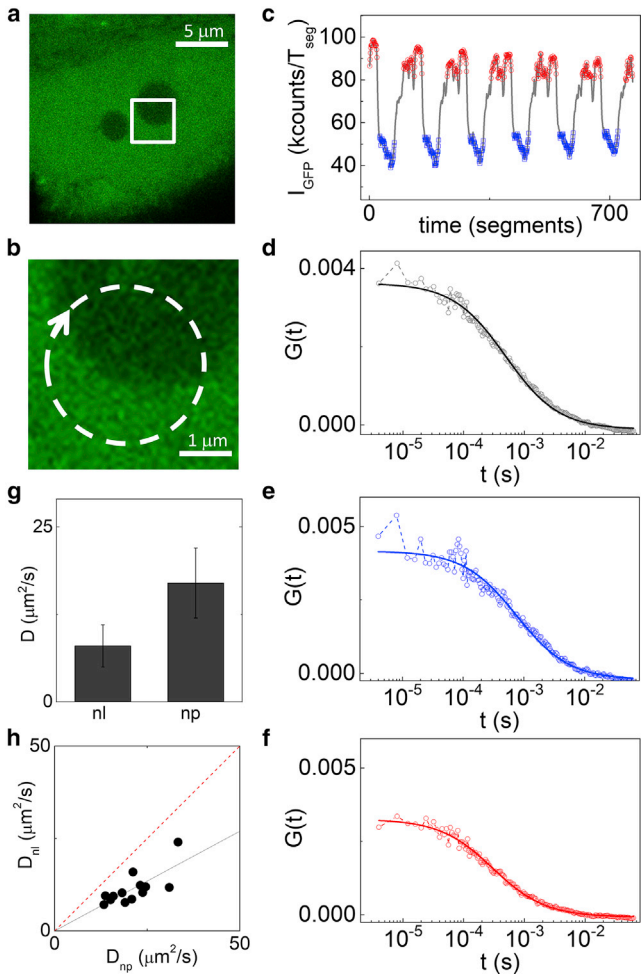

FIGURE 2 Measurement of GFP diffusion coefficient in the nucleoplasm and the nucleolus. Each measurement is performed on an individual cell (*a*), scanning the beams across the nucleolus (*b*). The GFP intensity trace is used for sorting the ACFs between the nucleolus (in *blue*) and the nucleoplasm (in *red*) (*c*). The total ACF without sorting (*d*) is compared to the sorted ACFs calculated from the fluctuations measured in the two regions (*e* and *f*). (*g*) The average values of diffusion coefficient of GFP in the nucleolus (nl) and nucleoplasm (np) was extracted from the fitting of the sorted ACFs (mean ± SD of n = 73 cells from five independent experiments). (*h*) Scatter plot of D_{nl} versus the value of D_{np} measured on the same cell is shown. Data represent measurements from different cells in a representative experiment. The solid black line is a linear fit with the intercept fixed to zero and slope 0.54 ± 0.04. The dashed red line represents the case in which the diffusion coefficients are the same in both the compartments. To see this figure in color, go online.

These results show, as expected, that the diffusion of GFP is reduced in the nucleolus with respect to the nucleoplasm because of higher molecular crowding. It is worth noting that we have not used the FCS segments corresponding to the interface between the two regions (Fig. 2 *c*) because they are expected to show a mixed behavior. However, the capability of measuring mobility of proteins at the boundary of nuclear domains could be

of interest for models of chromatin organization based on phase separation (43).

Measurement of GFP diffusion in euchromatin versus heterochromatin

Next, we checked if the technique was able to detect differences of GFP diffusion between regions of high and low chromatin density (hereafter referred to as hetero- and euchromatin) using as a reference the intensity of Hoechst-stained DNA (Fig. 3). First, we performed the measurements in the nucleoplasm of HeLa cells in regions far from the nucleolus (Fig. 3, *a* and *b*). In this way, we could use the Hoechst intensity as a quantitative reference for nuclear DNA concentration, defining regions of euchromatin (low Hoechst signal) and heterochromatin (high Hoechst signal) (Fig. 3 *c*) and to generate the corresponding ACFs (Fig. 3, *d* and *e*). We found that the absolute values of the diffusion coefficient of GFP in euchromatin, $D_{ec} = 23 \pm 7\ \mu m^2/s$, and heterochromatin, $D_{hc} = 20 \pm 6\ \mu m^2/s$, were similar when considering the average of measurements performed on multiple cells (mean ± SD of n = 72 cells from five independent experiments). Conversely, comparing each measured value of D_{hc} with the value of D_{ec} measured on the same cell (Fig. 3 *f*; Fig. S2), we found that the ratio between the diffusion coefficient in hetero- and euchromatin was less than one ($D_{hc}/D_{ec} = 0.87 \pm 0.05$, mean ± SD of five independent experiments with at least eight different cells per experiment). In fact, the single-cell sensitivity of our method facilitates stressing the differences in protein mobility within different chromatin regions, without being affected by the high intercellular variability.

Interestingly, we found a greater difference in the case of perinucleolar heterochromatin (Fig. 3, *g–k*). To focus on this region, we scanned the beams across the perinucleolar heterochromatin (Fig. 3, *g–h*) and used both the GFP and Hoechst intensities as references to discard the FCS segments belonging to the nucleolus (low GFP signal) and generate the ACFs corresponding to the perinucleolar heterochromatin (high GFP signal, high Hoechst signal) and the euchromatin (high GFP signal, low Hoechst signal) (Fig. 3, *i–k*). For the perinucleolar heterochromatin, we

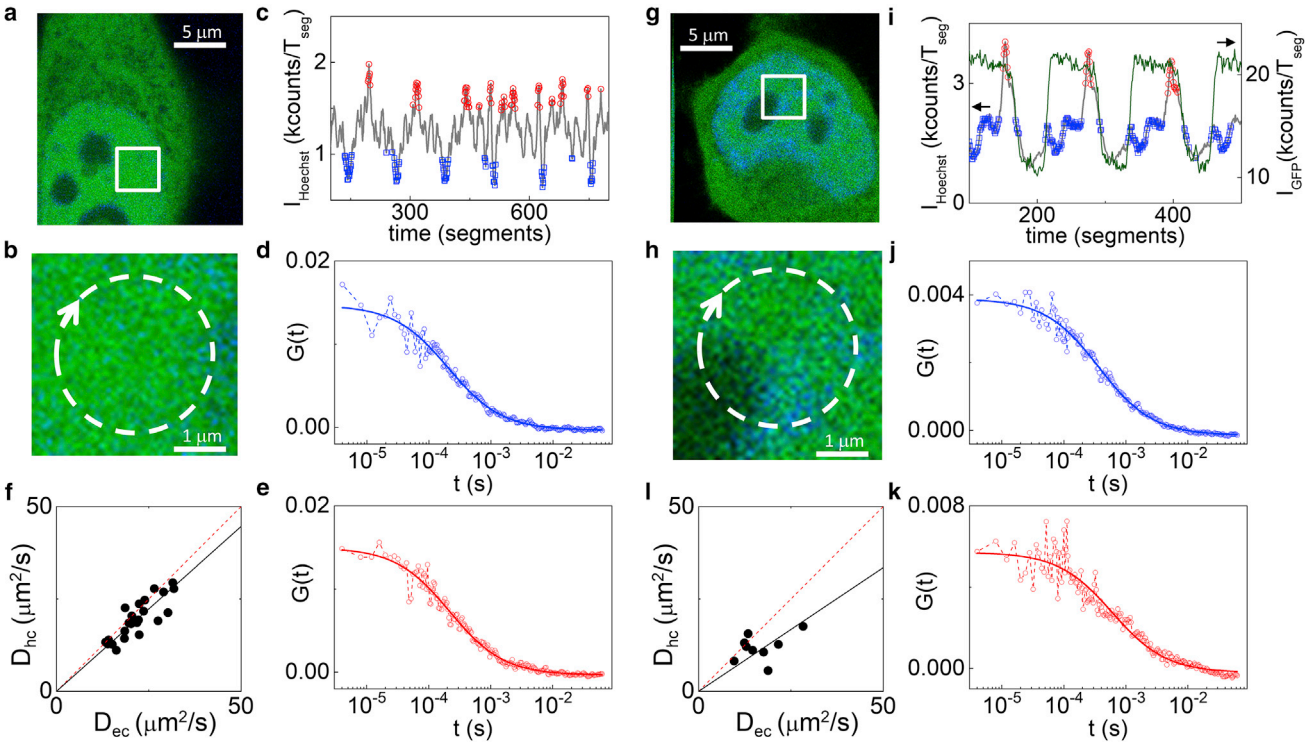

FIGURE 3 Measurement of the diffusion coefficient of untagged GFP in eu- versus heterochromatin (*a–f*) and in euchromatin versus perinucleolar heterochromatin (*g–k*). (*a* and *b*) Each measurement is collected from a single nucleus stained with Hoechst (in *blue* in (*a* and *b*)), far from the nucleolus. Based on the Hoechst intensity trace (*c*), the FCS segments are sorted into two populations: the heterochromatin, in red, and the euchromatin, in blue. (*d* and *e*) Shown are sorted ACFs associated to the euchromatin (*d*) and the heterochromatin (*e*) along with the corresponding single component pure diffusion model fits ((*d*) $D = 31.5\ \mu m^2/s$; (*e*) $D = 29.4\ \mu m^2/s$). (*f*) Scatter plot of D_{hc} versus the value of D_{ec} measured on the same cell is shown. Data represent measurements from different cells in a single experiment. The black solid line is a linear fit of the data with slope 0.89 ± 0.03. (*g–i*) For selecting the perinucleolar heterochromatin, the beams are scanned through the periphery of a nucleolus (*g* and *h*), and both the GFP (*green line*) and Hoechst (*gray line*) intensities are used as references (*i*). (*j* and *k*) Shown are sorted ACFs corresponding to the euchromatin (*j*) and perinucleolar heterochromatin (*k*), along with the corresponding single component pure diffusion model fits ((*j*) $D = 17.6\ \mu m^2/s$; (*k*) $D = 10.6\ \mu m^2/s$). (*l*) Scatter plot of D_{hc} versus D_{ec} for perinuclear heterochromatin is shown. Data represent measurements from different cells in a single experiment. The solid black line is a linear fit of the data with slope 0.7 ± 0.1. To see this figure in color, go online.

obtained a ratio of $D_{hc}/D_{ec} = 0.7 \pm 0.07$ (mean ± SD of four independent experiments with at least five different cells per experiment, Fig. 3 *l*; Fig. S3).

Previous FCS studies have been incapable of identifying differences in the mobility of monomeric GFP in nuclear compartments with different chromatin density (21). Our results show instead that even the motion of a small inert probe (monomeric GFP) is affected by the higher degree of compaction of the heterochromatin regions, especially in the perinucleolar heterochromatin. In this respect, we believe that a higher accuracy in our data may result, at least in part, from the following characteristics of our method. First of all, the high (microsecond) temporal resolution of the ACF ensures a proper sampling of the ACF, especially if compared to scanning FCS (millisecond temporal resolution). Second, the efficient sorting of the short FCS measurements ensures that fluctuations are averaged only between regions with the same intensity-based fingerprint (for instance, in the case of heterochromatin, these are only the regions identified by the Hoechst peaks), even if these regions are not completely immobile during the whole acquisition. This is conceptually similar to performing FCS on a tracked subcellular region (44–46), although this tracking is performed a posteriori on the recorded intensity profile. A similar idea has been exploited in the context of raster image correlation spectroscopy to perform fluctuation analysis on specific organelles (30). Finally, another advantage of our approach is the possibility of obtaining cell-by-cell estimates of the diffusion coefficients for each of the probed nuclear regions.

Monitoring the diffusion coefficient of GFP during chromatin compaction changes

To test to the extent that chromatin compaction affects GFP diffusion in different chromatin regions, we treated the cells with solutions known to induce changes in the compaction of chromatin.

Solutions of different osmolarities induced visible changes in nuclei morphology (Fig. 4, *a*, *e*, and *i*) that are reflected in a large difference in the diffusion coefficients of GFP measured in different compartments. Indeed, if the cells were treated with a hypo-osmolar solution, the diffusion coefficient of GFP was higher than in controls; when the cells were subjected to hyperosmolar treatment, the diffusion coefficients calculated in both eu- and heterochromatin were significantly lower ($D_{ec} = 7.2 \pm 2.3$ and $D_{hc} = 6.7 \pm 2.3$ $\mu m^2/s$, mean ± SD, n = 20 cells from two independent experiments) compared to the controls (Table 1).

Interestingly, both hypo- and hyperosmolar treatments affected only the absolute values of the diffusion coefficients but not their average ratio D_{hc}/D_{ec} (Fig. 4, *h* and *l*; Table 1), meaning that the treatment has a similar impact on both eu- and heterochromatin compartments.

Incubation with an ATP depletion solution induced a visible compaction of chromatin with respect to the control (Fig. 4, *a* and *m*), which led to a reduction of GFP diffusion coefficients in both eu- and heterochromatin (Table 1). In this case, however, the scatter plot of D_{hc} versus D_{ec} (Fig. 4 *p*) indicates that ATP depletion results in a more prominent slowdown of GFP diffusion in heterochromatin, possibly as a consequence of a larger increase of compaction in heterochromatin with respect to euchromatin, in keeping with previous studies (38).

Mobility of a transcription factor in different chromatin regions

As a model of a protein interacting with chromatin, we studied the mobility of the ER, a transcription factor member of the nuclear receptor superfamily and involved in the regulation of specific genes in response to hormone binding. In particular, we measured differences in the mobility of GFP-ER inside and outside an engineered, readily visible prolactin reporter gene "array" after stimulation with 10 nM 17-β-estradiol for 1 h (Fig. 5, *a* and *b*). Using GFP-ER intensity as a reference, we measured the diffusion inside (high GFP-ER signal) and outside (low GFP-ER signal) the array (Fig. 5 *c*). The intensity-sorted ACFs were fitted using either a two-component pure diffusion model (Fig. 5 *d*) or a Full Model (FM), taking into account diffusion and binding (15) (Fig. 5 *f*). Rigorously, because the ACFs do not decay to a baseline value (see below), the results obtained from the fits should not be interpreted quantitatively but only qualitatively.

In the first case, we identified a slow ($D_{slow} = 0.07$ $\mu m^2/s$) and a fast diffusing component ($D_{fast} = 2.1$ $\mu m^2/s$), in keeping with previous reports (2). We then plotted the slow fraction (SF), calculated as $SF = G_{0slow}/(G_{0slow} + G_{0fast})$, inside ($SF_{array}$) and outside ($SF_{np}$) the array (Fig. 5 *e*). As a result of the fit with the two-component diffusion model (Fig. 5 *d*), we found that the slow-diffusing fraction was significantly higher in the array compared to the nucleoplasm, with a ratio $SF_{array}/SF_{np} = 0.73 \pm 0.06$ (mean ± SD of three independent experiments with at least 19 different cells per experiment, Fig. 5 *e*; Fig. S6).

We then performed a fit of the data using the FM, which is more general and yields several outputs, including the number of particles (N), the bound fraction (BF), and the protein residence time (RT) on its binding site (15). The results of the analysis with this model are shown in (Fig. 5, *g–i*). Reflecting the increased density of estrogen response elements (EREs) at the engineered transcription locus, the number of ER molecules was higher in the array than in the nucleoplasm ($N_{np}/N_{array} = 0.67 \pm 0.03$, mean ± SD of three independent experiments, Fig. 5 *g*; Fig. S7). Also, the fraction of molecules in a bound state is significantly higher on the array ($BF_{np}/BF_{array} = 0.83 \pm 0.07$, mean ± SD of three independent experiments, Fig. 5 *h*; Fig. S7). Finally, the average time the ER is found in the bound state is longer on the array ($RT_{np}/RT_{array} = 0.65$

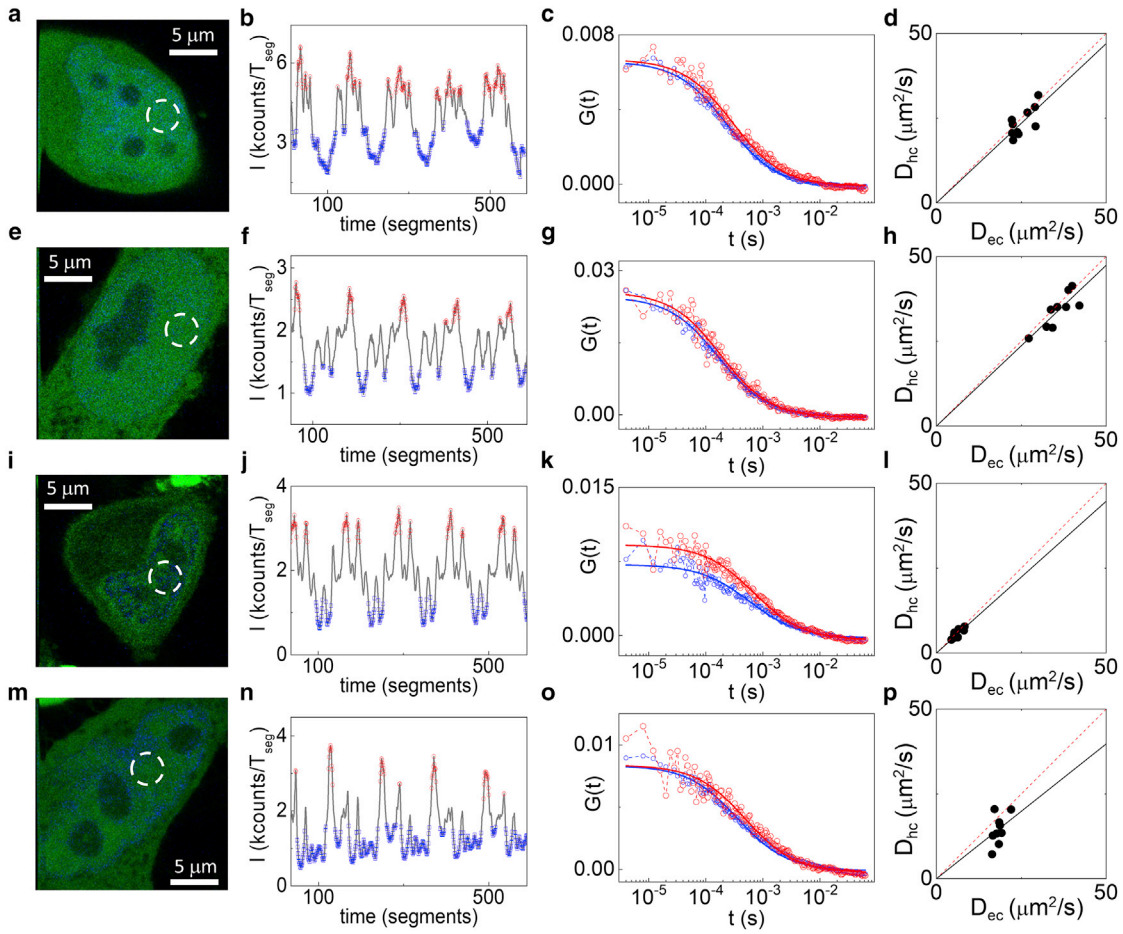

FIGURE 4 Measurement of the untagged-GFP diffusion coefficient after treatments affecting chromatin compaction state. All the measurements were performed comparing eu- and heterochromatin in the nucleoplasm of HeLa cells. (*a–d*) Shown are control cells, (*e–h*) cells treated with a hypo-osmolar solution, (*i–l*) cells treated with a hyperosmolar solution, (*m–p*) and cells treated with an ATP depletion solution. The FCS segments are sorted based on the Hoechst intensity level (*b*, *f*, *j*, and *n*), to obtain the sorted ACFs corresponding to euchromatin (*blue*) and heterochromatin (*red*) (*c*, *g*, *k*, and *o*). (*d*, *h*, *l*, and *p*) Scatter plots of D_{hc} versus D_{ec} along with the corresponding linear fits are shown. In each plot, data represent measurements from different cells in a single experiment. ((*d*) slope = 0.94 ± 0.04; (*h*) slope = 0.95 ± 0.03; (*l*) slope = 0.89 ± 0.04; (*p*) slope = 0.79 ± 0.07). To see this figure in color, go online.

± 0.04, mean ± SD of three independent experiments, Fig. 5 *i*; Fig. S7). These results show that not only is more ER targeted to the gene array (e.g., brighter signal), but also a larger fraction of ER is in a bound state—rather than freely diffusing—at the gene array. Although there are thousands of ER binding sites present throughout the nucleus, ERE density within the prolactin gene array recruits and retains the receptor longer than elsewhere in the nucleoplasm.

It is worth noting that, in this case, the sorted ACFs (Fig. 5, *d* and *f*) do not decay completely to a baseline value, probably because of the relatively short duration of the segments (T_{seg} = 1.05 s). This may affect the accuracy of the values extracted from the fits, especially on the array, in which the dynamics are slower. In other words, the scanning speed that we set in these experiments (v ∼ 0.07 μm/s) is still quite high compared to the slow dynamics observed on this system and, in particular, on the array.

Ideally, one would like to adapt the acquisition and analysis parameters to the diverse dynamics observable on different regions. This suggests a more efficient implementation of the method in which the scanning speed is varied during acquisition, and segments of different duration are used for sorting during analysis.

Measurements of GFP diffusion in the nucleolus and the nucleoplasm at subdiffraction spatial scales

Finally, we tested if the intensity-sorted approach was compatible with super-resolved FCS. Indeed, FCS can be combined with STED microscopy (STED-FCS) to perform fluctuation analysis on subdiffraction observation volumes (47). In STED, the size of observation volume can be easily tuned by changing the depletion power (48). Thus, an important aspect of STED-FCS is the capability to probe diffusion

TABLE 1 Values of the Average Diffusion Coefficient of Untagged GFP in Eu- and Heterochromatin and Average Value of the Ratio D_{hc}/D_{ec} between the Two Diffusion Coefficients Measured in the Same Cell

	D_{ec} ($\mu m^2/s$)	D_{hc} ($\mu m^2/s$)	D_{hc}/D_{ec}
Control	23 ± 7	20 ± 6	0.87 ± 0.05
ATP depletion	18 ± 4	15 ± 5	0.79 ± 0.08
Hyperosmotic	7.2 ± 2	6.7 ± 2	0.92 ± 0.03
Hypoosmotic	30.1 ± 8	29.6 ± 7	0.98 ± 0.03

Values of D_{ec} and D_{hc} represent mean ± SD from at least 20 cells. Values of D_{hc}/D_{ec} represent mean ± SD of the slope values calculated in at least two independent experiments with at least eight cells per experiment.

at different subdiffraction spatial scales (i.e., to perform a spot-variation FCS analysis), just by changing the depletion power (49). Alternatively, the STED observation volume can be tuned, at a given STED power, by exploiting the fluorescence lifetime variations generated in a CW-STED microscope (50,51). This strategy has the advantage that a full spot-variation data set can be obtained in a single measurement, without the need of performing multiple acquisitions at different depletion powers (52). Following this strategy, we recently demonstrated that, by combining the analysis of lifetime variations generated in a CW-STED microscope (51) with fluorescence lifetime correlation spectroscopy (41), it is possible to perform STED-based spot-variation FCS in single points in the interior of the cell (40).

We coupled this method with intensity-sorted FCS. The measurements were done in HeLa cells, with the scan orbit passing across the nucleolus and using as a reference the GFP intensity level (Fig. 6, *a* and *b*). The GFP lifetime variations induced by the STED laser beam were used to filter the detected photons, identifying in this way three different effective volumes (Fig. S8) in the same measurement (40).

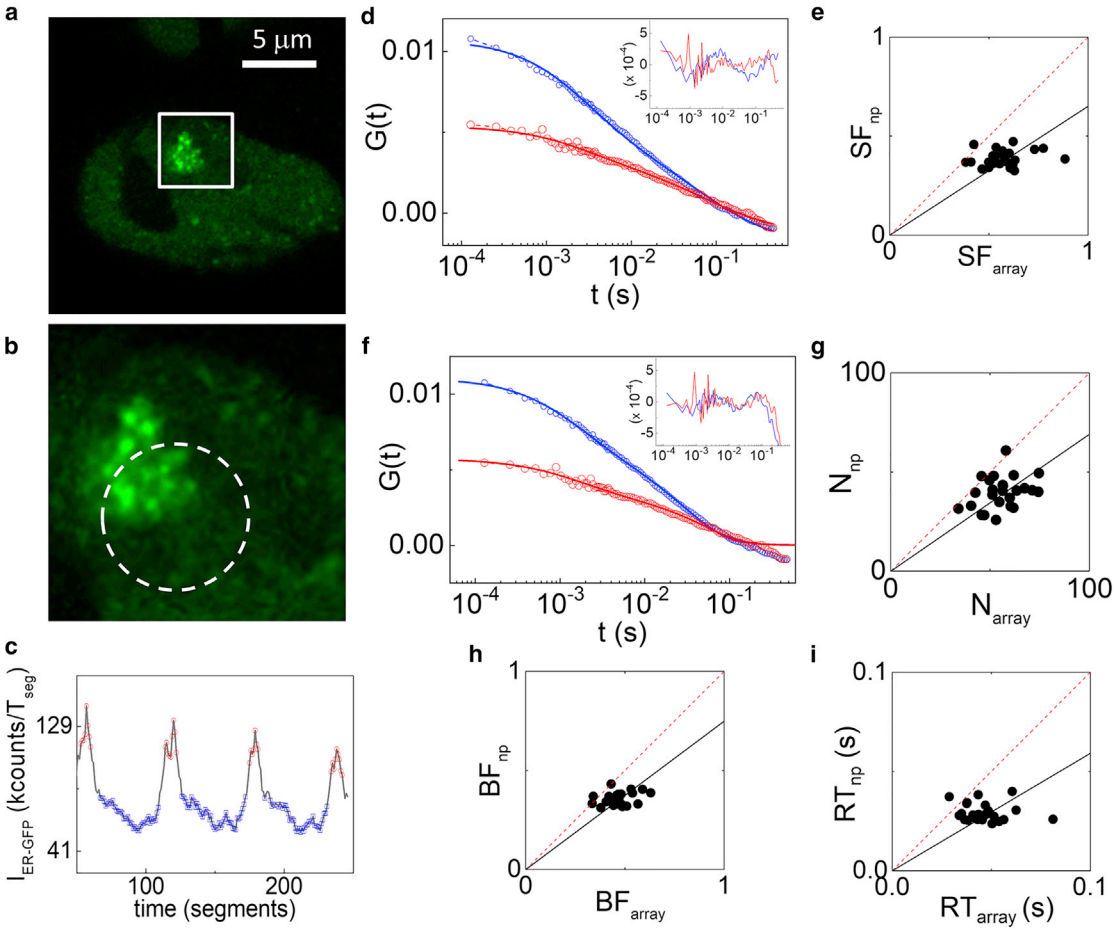

FIGURE 5 Measurement of the mobility of the estrogen receptor (ER) inside and outside an engineered prolactin gene array. (*a* and *b*) The measurements were performed orbiting across the prolactin gene array. (*c*) The intensity of the GFP-ER signal is used as a reference for sorting the ACFs corresponding to the array (*red*) and to the nucleoplasm (*blue*). (*d* and *e*) Analysis with a two-diffusion component model is shown. (*d*) A global fit performed on the sorted ACFs (*red*: sorted ACF of the array, *blue*: sorted ACF of the nucleoplasm) yields a shared value of diffusion coefficients $D_{slow} = 0.07\ \mu m^2/s$ for the slow-diffusing population and $D_{fast} = 2.1\ \mu m^2/s$ for the fast diffusing one. (*e*) Scatter plot of the SF was calculated in the two probed nuclear regions. The solid black line is a linear fit of the data with intercept fixed and with slope 0.65. (*f–i*) Analysis with the FM, showing the fitted ACFs (*f*) and the scatter plots of the number of proteins (*g*), the BF (*h*), and the RT (*i*) for the nucleoplasm and for the array, along with the corresponding linear fits ((*g*) slope = 0.69; (*h*) slope = 0.75; (*i*) slope = 0.59). Residuals are shown as plot insets in (*d* and *f*). To see this figure in color, go online.

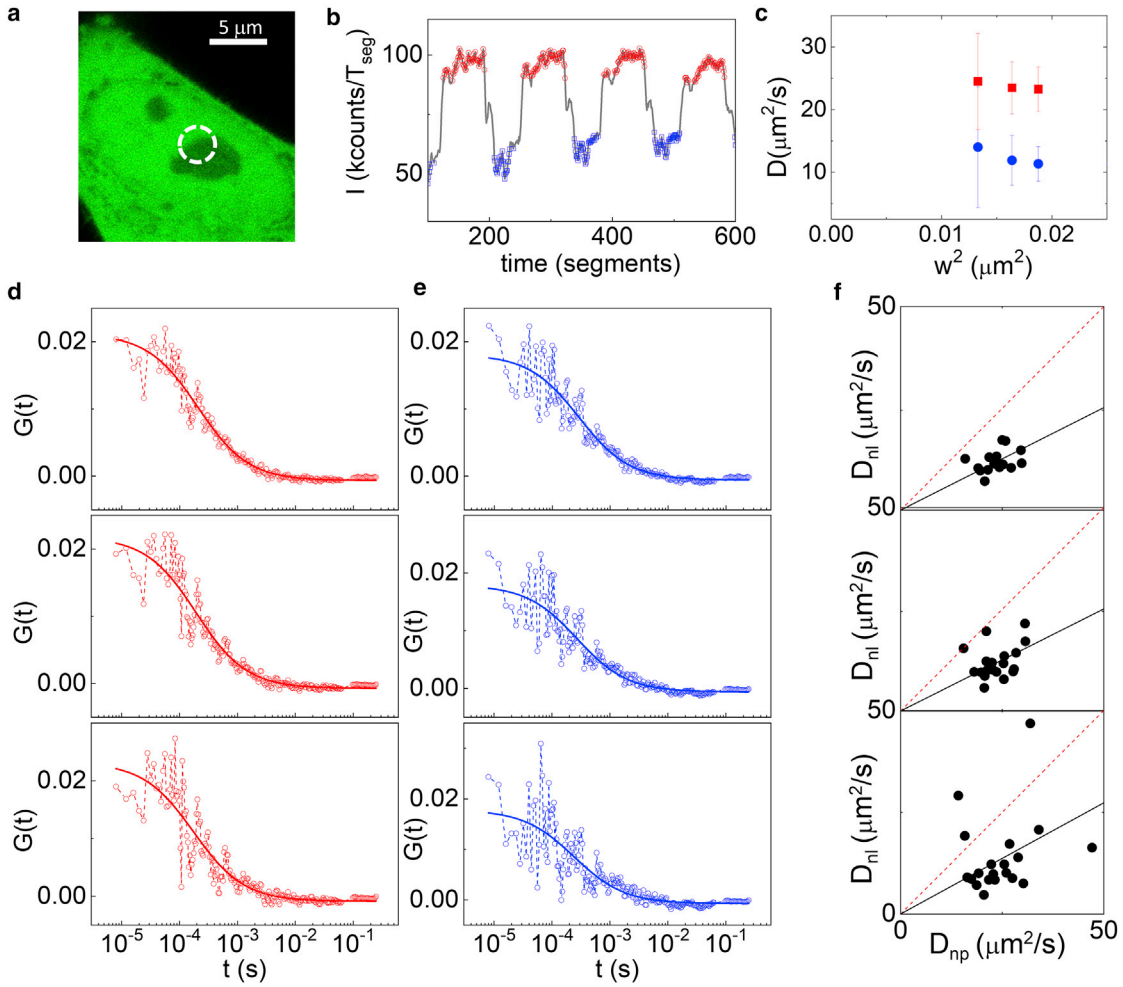

FIGURE 6 Intensity-sorted STED-FCS in the nucleus. Each measurement is performed on an individual cell, scanning the beams across the nucleoli (*a*). (*b*) GFP intensity trace was used for sorting the ACFs between the nucleolus (in *blue*) and the nucleoplasm (*red*). Three different volumes are selected in the postprocessing, with beam spot size w = 140, 130, and 115 nm, respectively. (*d* and *e*) Shown are ACFs corresponding to detection volumes of decreasing size (from *top* to *bottom*) along with the fit, for the nucleoplasm (D_{np} = 30; 32; 35 $\mu m^2/s$ from *top* to *bottom*) (*d*) and the nucleolus (D_{nl} = 22; 23; 26 $\mu m^2/s$ from *top* to *bottom*) (*e*). (*c*) Shown is the average diffusion coefficient versus the square of the spot waist, for GFP in the nucleoplasm (*red*) and in the nucleolus (*blue*) (data represent mean ± SD of n = 20 measurements on different cells). (*f*) Scatter plots of D_{nl} versus D_{np}, for each effective detection volume, together with the corresponding linear fits (slope = 0.48; 0.5; 0.55 from *top* to *bottom*) are shown. To see this figure in color, go online.

The sorting of the data generated, for each cell, two sets of ACFs, corresponding to the nucleoplasm (Fig. 6 *c*) and the nucleolus (Fig. 6 *d*). This corresponds to a separate spot-variation analysis for each compartment, shown as the average diffusion coefficient versus the square size of the effective observation volume (Fig. 6 *e*). At smaller spatial scales, we observed a slight increase of the diffusion coefficient, especially in the nucleolus, but also a much larger error bar. This is probably due not only to cell-to-cell variability but also the fact that reducing the size of the effective detection volume (w_{eff} = 140, 130, and 115 nm, from *top* to *bottom*) results in ACFs with a poorer signal/noise ratio (Fig. 6, *c* and *d*). We tested whether the ratio between the diffusion coefficient in the nucleolus versus nucleoplasm was also preserved at different subdiffraction spatial scales on a cell-by-cell basis (Fig. 6 *f*). The results are in keeping with those obtained with confocal intensity-sorted FCS (Fig. 2), despite a higher scattering of the diffusion coefficient values that are probably ascribed to the signal-to-noise ratio reduction of the ACFs at the smallest effective observation volumes.

Taken together, these results show the compatibility of our approach with STED and that, in principle, intensity-sorted STED-FCS could be a useful tool to measure mobility in different nuclear regions at multiple subdiffraction spatial scales. Note that the high temporal resolution allows an optimal temporal sampling of the ACF even if the average transit time measured in the nucleoplasm at the smaller effective observation volume is in the order of 100 μs. The major limitation we encountered was related to the poor quality of the ACFs at smaller observation volumes. This aspect could be improved by using

probes that are brighter and/or more photostable than GFP, for example, using the genetically encoded Halo or SNAP tags that allow the use of brighter, more stable organic dyes. The increase in the number of photons collected could facilitate pushing the spot-variation analysis toward smaller spatial scales.

Finally, it is worth noting that STED, by providing intensity features that are better resolved spatially, should also improve the sorting of the data. In our test system (i.e., nucleolus versus nucleoplasm), we did not exploit this advantage because the two regions extend over several micrometers and are easily distinguished with normal resolution. Moreover, by averaging all the segments within each compartment, we are prevented from detecting any spatial and temporal heterogeneity within each region. However, this is an interesting aspect that might be worth future investigations.

CONCLUSIONS

In this study, we proposed a solution to the unique challenges encountered by FCS-based methods aimed at probing nuclear mobility without the loss of spatial information. This method is based on slow, continuous line-scanning FCS, which is capable of sampling different nuclear positions while keeping a high temporal resolution. A key aspect of the method is the use of a reference intensity trace to sort segments of the whole FCS measurement into two or more populations corresponding to specific nuclear regions.

We used this method to probe the diffusion of inert GFP in different nuclear domains. As expected, the diffusion was slowed down in the nucleolus relative to the nucleoplasm, presumably because of higher molecular crowding. More interestingly, when studying the GFP mobility in hetero- versus euchromatin, we found a slight difference between the diffusion coefficients, which is increased when compared to perinucleolar heterochromatin. A variation of the mobility of GFP was also appreciable when using treatments that alter chromatin structure. These results indicate that, even for a small inert probe like GFP, chromatin and its compaction states can markedly influence diffusion rates, allowing the possibility of using such small inert probes to study chromatin organization and nuclear rheology in living cells. Because of the single-cell sensitivity of our method, we were able to highlight intracellular variations of mobility between different chromatin regions despite a high intercellular variability.

We also showed the applicability of our method in the study of proteins that interact with chromatin, bringing as an interesting example intranuclear mobility of the ER. We were able to discriminate between diffusion measured at an engineered prolactin gene array (e.g., transcription locus), in which the number of EREs and receptor proteins is higher than in the nucleoplasm. Interestingly, we also retrieved important information about the binding and the RT of the proteins on the array versus the other binding sites scattered throughout the nucleoplasm.

Finally, we coupled our intensity-sorted FCS method with STED microscopy, demonstrating the possibility to probe different nuclear regions at subdiffraction spatial scales. In addition, because of the efficient postprocessing tuning of detection volumes, we were able to obtain a spot-variation analysis specific for each compartment in the same measurement.

In summary, we proposed a new, statistically robust method that can be used to perform accurate mobility measurements at microsecond temporal resolution in different compartments, without the constraint of having the probed regions nearly immobile during FCS measurements. In addition, intensity-sorted FCS is suitable to study the diffusion of small inert probes but also the interaction of proteins with a slowly moving substrate. We believe that this method, especially if coupled with super-resolution, will be useful to study the dynamics of chromatin at the nanoscale, eventually leading to interesting insights into nuclear structure-function relationships.

SUPPORTING MATERIAL

Eight figures are available at http://www.biophysj.org/biophysj/supplemental/S0006-3495(19)30130-4.

AUTHOR CONTRIBUTIONS

L.L., A.D., and G.V. designed research. M.D.B. prepared samples and performed experiments. L.L. wrote software. All authors analyzed data and discussed results. M.D.B. and L.L. wrote the manuscript with input from A.D., G.V., D.M., and M.A.M.

ACKNOWLEDGMENTS

Imaging work was performed at the Nikon Imaging Center at Istituto Italiano di Tecnologia, generously supported by Nikon. The authors wish to thank Maureen G. Mancini for development of the GFP-ER:PRL-HeLa cell line. The authors also wish to thank G. Tortarolo for technical support.

L.L. was supported by Fondazione Cariplo and Associazione Italiana per la Ricerca sul Cancro through Trideo (Transforming Ideas in Oncological Research) grant number 17215. D.M. was supported by Fondazione Cariplo (Ricerca Biomedica condotta da giovani ricercatori, 2014-1157). M.A.M. was supported with funding from NIEHS (ES027704), NIH (DK56338 and CA125123), CPRIT (RP150578, RP170719), and the Dan L. Duncan Comprehensive Cancer Center.

REFERENCES

1. McNally, J. G., W. G. Müller, …, G. L. Hager. 2000. The glucocorticoid receptor: rapid exchange with regulatory sites in living cells. *Science.* 287:1262–1265.

2. Stenoien, D. L., K. Patel, …, M. A. Mancini. 2001. FRAP reveals that mobility of oestrogen receptor-α is ligand- and proteasome-dependent. *Nat. Cell Biol.* 3:15–23.

3. Misteli, T. 2001. Protein dynamics: implications for nuclear architecture and gene expression. *Science.* 291:843–847.
4. Phair, R. D., and T. Misteli. 2000. High mobility of proteins in the mammalian cell nucleus. *Nature.* 404:604–609.
5. Magde, D., E. Elson, and W. W. Webb. 1972. Thermodynamic fluctuations in a reacting system measurement by fluorescence correlation spectroscopy. *Phys. Rev. Lett.* 29:705–708.
6. Mazza, D., A. Abernathy, …, J. G. McNally. 2012. A benchmark for chromatin binding measurements in live cells. *Nucleic Acids Res.* 40:e119.
7. Bancaud, A., S. Huet, …, J. Ellenberg. 2009. Molecular crowding affects diffusion and binding of nuclear proteins in heterochromatin and reveals the fractal organization of chromatin. *EMBO J.* 28:3785–3798.
8. Erdel, F., K. Müller-Ott, …, K. Rippe. 2011. Dissecting chromatin interactions in living cells from protein mobility maps. *Chromosome Res.* 19:99–115.
9. Annibale, P., and E. Gratton. 2014. Advanced fluorescence microscopy methods for the real-time study of transcription and chromatin dynamics. *Transcription.* 5:e28425.
10. Misteli, T. 2008. Physiological importance of RNA and protein mobility in the cell nucleus. *Histochem. Cell Biol.* 129:5–11.
11. Meshorer, E., D. Yellajoshula, …, T. Misteli. 2006. Hyperdynamic plasticity of chromatin proteins in pluripotent embryonic stem cells. *Dev. Cell.* 10:105–116.
12. Ries, J., and P. Schwille. 2012. Fluorescence correlation spectroscopy. *BioEssays.* 34:361–368.
13. Vivante, A., E. Brozgol, …, Y. Garini. 2017. Genome organization in the nucleus: from dynamic measurements to a functional model. *Methods.* 123:128–137.
14. Chen, Y., J. D. Müller, …, E. Gratton. 2002. Molecular brightness characterization of EGFP in vivo by fluorescence fluctuation spectroscopy. *Biophys. J.* 82:133–144.
15. Michelman-Ribeiro, A., D. Mazza, …, J. G. McNally. 2009. Direct measurement of association and dissociation rates of DNA binding in live cells by fluorescence correlation spectroscopy. *Biophys. J.* 97:337–346.
16. Wachsmuth, M., W. Waldeck, and J. Langowski. 2000. Anomalous diffusion of fluorescent probes inside living cell nuclei investigated by spatially-resolved fluorescence correlation spectroscopy. *J. Mol. Biol.* 298:677–689.
17. Müller, K. P., F. Erdel, …, K. Rippe. 2009. Multiscale analysis of dynamics and interactions of heterochromatin protein 1 by fluorescence fluctuation microscopy. *Biophys. J.* 97:2876–2885.
18. Park, H., S. S. Han, …, C. G. Pack. 2015. Dynamic and unique nucleolar microenvironment revealed by fluorescence correlation spectroscopy. *FASEB J.* 29:837–848.
19. Tsutsumi, M., H. Muto, …, T. Aizawa. 2016. In vivo fluorescence correlation spectroscopy analyses of FMBP-1, a silkworm transcription factor. *FEBS Open Bio.* 6:106–125.
20. Cardarelli, F., L. Lanzano, and E. Gratton. 2011. Fluorescence correlation spectroscopy of intact nuclear pore complexes. *Biophys. J.* 101:L27–L29.
21. Dross, N., C. Spriet, …, J. Langowski. 2009. Mapping eGFP oligomer mobility in living cell nuclei. *PLoS One.* 4:e5041.
22. Roth, C. M., P. I. Heinlein, …, D. P. Herten. 2007. Imaging diffusion in living cells using time-correlated single-photon counting. *Anal. Chem.* 79:7340–7345.
23. Singh, A. P., R. Galland, …, T. E. Saunders. 2017. 3D protein dynamics in the cell nucleus. *Biophys. J.* 112:133–142.
24. Capoulade, J., M. Wachsmuth, …, M. Knop. 2011. Quantitative fluorescence imaging of protein diffusion and interaction in living cells. *Nat. Biotechnol.* 29:835–839.
25. Papadopoulos, D. K., A. J. Krmpot, …, V. Vukojević. 2015. Probing the kinetic landscape of Hox transcription factor-DNA binding in live cells by massively parallel Fluorescence Correlation Spectroscopy. *Mech. Dev.* 138:218–225.
26. Baum, M., F. Erdel, …, K. Rippe. 2014. Retrieving the intracellular topology from multi-scale protein mobility mapping in living cells. *Nat. Commun.* 5:4494.
27. Stortz, M., D. M. Presman, …, V. Levi. 2017. Mapping the dynamics of the glucocorticoid receptor within the nuclear landscape. *Sci. Rep.* 7:6219.
28. Hinde, E., F. Cardarelli, …, E. Gratton. 2010. In vivo pair correlation analysis of EGFP intranuclear diffusion reveals DNA-dependent molecular flow. *Proc. Natl. Acad. Sci. USA.* 107:16560–16565.
29. Scipioni, L., M. Di Bona, …, L. Lanzanò. 2018. Local raster image correlation spectroscopy generates high-resolution intracellular diffusion maps. *Commun Biol.* 1:10.
30. Hendrix, J., T. Dekens, …, D. C. Lamb. 2016. Arbitrary-region raster image correlation spectroscopy. *Biophys. J.* 111:1785–1796.
31. Mascetti, G., L. Vergani, …, C. Nicolini. 1996. Effect of fixatives on calf thymocytes chromatin as analyzed by 3D high-resolution fluorescence microscopy. *Cytometry.* 23:110–119.
32. Kis-Petikova, K., and E. Gratton. 2004. Distance measurement by circular scanning of the excitation beam in the two-photon microscope. *Microsc. Res. Tech.* 63:34–49.
33. Lanzanò, L., and E. Gratton. 2014. Orbital single particle tracking on a commercial confocal microscope using piezoelectric stage feedback. *Methods Appl. Fluoresc.* 2:1–19.
34. Ranjit, S., L. Lanzano, and E. Gratton. 2014. Mapping diffusion in a living cell via the phasor approach. *Biophys. J.* 107:2775–2785.
35. Vicidomini, G., I. C. Hernández, …, A. Diaspro. 2014. Gated CW-STED microscopy: a versatile tool for biological nanometer scale investigation. *Methods.* 66:124–130.
36. Curcio, A., R. Marotta, …, T. Pellegrino. 2012. Magnetic pH-responsive nanogels as multifunctional delivery tools for small interfering RNA (siRNA) molecules and iron oxide nanoparticles (IONPs). *Chem. Commun. (Camb.).* 48:2400–2402.
37. Stossi, F., M. J. Bolt, …, M. A. Mancini. 2014. Defining estrogenic mechanisms of bisphenol A analogs through high throughput microscopy-based contextual assays. *Chem. Biol.* 21:743–753.
38. Llères, D., J. James, …, A. I. Lamond. 2009. Quantitative analysis of chromatin compaction in living cells using FLIM-FRET. *J. Cell Biol.* 187:481–496.
39. Albiez, H., M. Cremer, …, T. Cremer. 2006. Chromatin domains and the interchromatin compartment form structurally defined and functionally interacting nuclear networks. *Chromosome Res.* 14:707–733.
40. Lanzanò, L., L. Scipioni, …, G. Vicidomini. 2017. Measurement of nanoscale three-dimensional diffusion in the interior of living cells by STED-FCS. *Nat. Commun.* 8:65.
41. Kapusta, P., M. Wahl, …, J. Enderlein. 2007. Fluorescence lifetime correlation spectroscopy. *J. Fluoresc.* 17:43–48.
42. Gröner, N., J. Capoulade, …, M. Wachsmuth. 2010. Measuring and imaging diffusion with multiple scan speed image correlation spectroscopy. *Opt. Express.* 18:21225–21237.
43. Strom, A. R., A. V. Emelyanov, …, G. H. Karpen. 2017. Phase separation drives heterochromatin domain formation. *Nature.* 547:241–245.
44. Lanzano, L., T. Lei, …, J. Blaine. 2011. Differential modulation of the molecular dynamics of the type IIa and IIc sodium phosphate cotransporters by parathyroid hormone. *Am. J. Physiol. Cell Physiol.* 301:C850–C861.
45. Cardarelli, F., L. Lanzano, and E. Gratton. 2012. Capturing directed molecular motion in the nuclear pore complex of live cells. *Proc. Natl. Acad. Sci. USA.* 109:9863–9868.
46. Annibale, P., and E. Gratton. 2015. Single cell visualization of transcription kinetics variance of highly mobile identical genes using 3D nanoimaging. *Sci. Rep.* 5:9258.

47. Kastrup, L., H. Blom, …, S. W. Hell. 2005. Fluorescence fluctuation spectroscopy in subdiffraction focal volumes. *Phys. Rev. Lett.* 94:178104.

48. Sarmento, M. J., M. Oneto, …, L. Lanzanò. 2018. Exploiting the tunability of stimulated emission depletion microscopy for super-resolution imaging of nuclear structures. *Nat. Commun.* 9:3415.

49. Eggeling, C., C. Ringemann, …, S. W. Hell. 2009. Direct observation of the nanoscale dynamics of membrane lipids in a living cell. *Nature*. 457:1159–1162.

50. Vicidomini, G., G. Moneron, …, S. W. Hell. 2011. Sharper low-power STED nanoscopy by time gating. *Nat. Methods.* 8:571–573.

51. Lanzanò, L., I. Coto Hernández, …, G. Vicidomini. 2015. Encoding and decoding spatio-temporal information for super-resolution microscopy. *Nat. Commun.* 6:6701.

52. Vicidomini, G., H. Ta, …, C. Eggeling. 2015. STED-FLCS: an advanced tool to reveal spatiotemporal heterogeneity of molecular membrane dynamics. *Nano Lett.* 15:5912–5918.